Article

Atmospheric and Oceanic Patterns Associated with Extreme Drought Events over the Paraná Hydrographic Region, Brazil

Aline Araújo de Freitas [1], Michelle Simões Reboita [1], Vanessa Silveira Barreto Carvalho [1], Anita Drumond [2], Simone Erotildes Teleginski Ferraz [3], Benedito Cláudio da Silva [1] and Rosmeri Porfírio da Rocha [2,*]

[1] Instituto de Recursos Naturais, Departamento de Ciências Atmosféricas, Universidade Federal de Itajubá, Itajubá 37500-903, Brazil
[2] Instituto de Astronomia, Geofísica e Ciências Atmosféricas, Departamento de Ciências Atmosféricas, Universidade de São Paulo, São Paulo 05508-090, Brazil
[3] Centro de Ciências Naturais e Exatas, Departamento de Física, Universidade Federal de Santa Maria, Santa Maria 97105-900, Brazil
[*] Correspondence: rosmerir.rocha@iag.usp.br

Abstract: The Paraná Hydrographic Region (PHR) is one of the main hydrographic basins in Brazil, standing out for its energy generation and consumption, among other ecosystem services. Thus, it is important to identify hydrological drought events and the driest periods inside of these droughts to understand the anomalous atmospheric circulation patterns associated with them (a multiscale study). This study used the standardized precipitation index (SPI) for the 12-month scale to identify hydrological drought episodes in the PHR from 1979 to 2021. For these episodes, the severity, duration, intensity, and peak were obtained, and the SPI-6 was applied to the longest and most severe drought to identify periods with dry conditions during the wet season. Anomalous atmospheric and oceanic patterns associated with such episodes were also analyzed. The results reveal that the longest and most severe hydrological drought on the PHR started in 2016. The end of this episode was not identified by the end of the analyzed period. The SPI-6 revealed three rainy seasons during this drought event marked by anomalous dry conditions: 2016/2017, 2019/2020, and 2020/2021. In general, the circulation patterns identified differ in each period, for example, in 2016/2017, an El Niño event was dominant, in 2019/2020, the tropical Pacific Ocean showed neutral conditions, and in 2020/2021, a La Niña episode was registered. Despite that, in the three periods, the anomalous atmospheric patterns contributed to the weakening of the low-level jet east of the Andes and, consequently, to the decreasing of the moisture transport to the PHR, then leading to dry conditions over the basin.

Keywords: Paraná Hydrographic Region; SPI; precipitation deficit

1. Introduction

In recent years, extreme events, characterized as typical weather or climate conditions that occur in a given location and cause damage to people, property, and nature, showed greater frequency, duration, and intensity [1–4]. According to the Summary for Policymakers of the Sixth Assessment Report of the Intergovernmental Panel on Climate Change [2], human-induced climate change affected extreme climate events in several regions of the globe, and in the future, increases are projected, especially in extreme events that combine factors and hazards that contribute to social or environmental risk, as, for example, the simultaneous occurrence of heat waves and drought.

In Brazil, droughts, which account for approximately 48% of all disasters, affected the largest number of people between 1991 and 2012; around 64 million people [5]. The most affected regions in the country are the Northeast of Brazil and Southern Brazil with 60% and 27% of the natural disaster occurrence records, respectively [5]. It is important to highlight that drought can be defined simply as a water deficit compared to normal conditions,

but in general, they are considered a complex problem that can have different meanings and effects depending on the affected sector, such as agriculture, water management, and hydroelectric systems [6,7]. They can be classified into meteorological, agricultural, hydrological, and socioeconomic droughts, according to the associated impact [7,8]. In total, natural disasters in Brazil resulted in losses of approximately USD 37 billion for the country between 1995 and 2019, with agriculture being the most affected sector of the economy (about USD 22 billion of losses) [9]. Additionally, according to Schadeck [9], from 1995 to 2019, there is a trend of increasing damage and losses caused by droughts, with the 2010s being responsible for approximately 66.5% of the economic losses.

To facilitate the identification of the beginning, location, severity, and end of drought conditions, different stages of the hydrological cycle can be monitored with the help of different indices and indicators, since there are several causes and impacts caused by those events [10]. Five indices are more frequently used in Brazil for this end [10]: the Palmer drought severity index, standardized precipitation–evapotranspiration index, crop moisture index, deciles, quintiles, and crop-specific drought indices. Although there are different types of methods to study droughts, each with its respective advantages and limitations (Table 1), in Brazil, the SPI, depending exclusively on precipitation, was applied in many studies for the evaluation of hydrological droughts, considering the 12-month scale of the index [11–15].

The largest water demand in Brazil, approximately 31% of the country's total demand, comes from the Paraná Hydrographic Region (PHR; Figure 1), with its main use for irrigation, industries, and urban supply [16–18]. The PHR has great national importance since it is located in the region with the greatest economic development in the country, comprising parts of the South, Southeast, and Center-West regions of Brazil (Figure 1). However, climate studies in the PHR showed negative trends toward precipitation anomalies in the northern region of the basin, with an increase in the number of consecutive dry days, and positive trends in the southern part of the basin, with increases in extreme precipitation events (>50 mm d^{-1}) [19,20]. In the last decade, Cuartas [20] also found standardized precipitation–evapotranspiration index (SPEI) and standardized precipitation index (SPI) values indicating severe to intense drought conditions in most of the PHR and low volumes of precipitation in the north/east region of the basin since 2014. This area is located in the SEB, which presented a serious water crisis in 2014/2015 [21–24]. These studies suggested the frequency and intensity of droughts are related to climate change, given the combination of reduced precipitation and increased temperature.

The Itaipu Hydroelectric Power Plant, for example, the largest generator of clean and renewable energy in the world, is located in the PHR. Being a binational entity, it was administered by Brazil and Paraguay since 1984 (the beginning of its operation) and, until 2018, it generated more than 2.6 billion MWh. However, Itaipu registered the lowest historical affluence value in 2020 [25,26]. Fernandes et al. [27] showed that the rainfall deficit in 2019/2020 impacted, in addition to agro-productive areas, the water resources of the Southern Brazil region. Using the SPI and standardized flow (SSFI) indices, the authors found drought conditions in all municipalities in the Southern Brazil region during the first quarter of 2020.

Several economic sectors were impacted by the droughts in the PHR in recent years, especially in 2019/2020 [28,29]. The National Water and Sanitation Agency (ANA) published in June 2021 a resolution to declare a critical scarcity of water resource availability of the PHR associated with precipitation deficits starting in 2019 [30]. Due to the low levels of the Paraná River, the Tietê-Paraná waterway—which connects producing areas, mainly in the agricultural sector, in the states of São Paulo, Paraná, Minas Gerais, Mato Grosso do Sul, and Goiás, to the maritime ports, serving the main centers of Mercosur [31]—was closed from August 2021 to March 2022 [32–35].

In the PHR, different atmospheric systems are responsible for causing rain throughout the year, such as: (1) frontal systems, characterized by the contact between two air masses with different thermal properties; (2) pre-frontal squall lines, characterized by a line-shaped

cluster of clouds ahead of a cold front; (3) mesoscale convective systems (convective cloud agglomeration), such as mesoscale convective complexes with a circular shape and short life cycle, which have the low-level jets (LLJ) east of the Andes as the main moisture source for heavy rains; (4) synoptic-scale cyclones, which are low atmospheric pressure systems whose circulation is clockwise in the southern hemisphere, and (5) breeze circulations, generated due to differential heating between land and ocean [36,37]. The rainfall is distributed throughout the year in the southernmost region of the PHR [36,37]. In the northernmost region of the basin, the climate is quite similar to conditions observed in the Southeast region of Brazil, with drier winter months and rainier summer months, typical of the South American Monsoon System [38]. In the wettest months, one of the main responsible systems for causing a high volume of rain in the northern region of the basin is the South Atlantic Convergence Zone (SACZ). Characterized by a band of nebulosity oriented in the northwest-southeast direction from Southern Amazonia to southeastern Brazil; the SACZ is formed by the local convection and the convergence of northeast winds from the South Atlantic Subtropical Anticyclone (SASA), which brings moisture from the Atlantic Ocean towards the continent, and LLJ east of the Andes, which is responsible for transporting heat and humidity from the Amazon region to the southeast [36,37].

Changes in the PHR precipitation regime may be related to the large-scale phenomena influence of the frequency and intensity of the previously mentioned atmospheric systems. It is supported by the fact that some drought events were observed under the influence of the (a) Southern Annular Mode or Antarctic Oscillation, (b) La Niña phenomenon, and even (c) sea surface temperatures of the Tropical South Atlantic [27,29,39]. Although drought episodes are associated with natural climate variability, climate change can affect many of these phenomena. Studies on the influence of climate change on precipitation patterns showed that, for Southern Brazil, seasonal precipitation is expected to increase, while increases in extreme rainfall events are expected for southeastern Brazil, interposed with longer drought periods [40–43]. Hence, precipitation rates for the southern region of the PHR can become higher in the austral summer months, generating an increase in flow between 10 and 40% [41,44].

Therefore, considering the magnitude of the socioeconomic impacts of recent drought events in the main Brazilian river basins, mainly in the PHR, it is extremely important to understand the physical mechanisms that contribute to anomalies in the circulation pattern leading to droughts episodes, especially regarding the analysis of mechanisms linked to large-scale patterns. Thus, the objectives of this study are: (a) through SPI-12, to characterize the drought event that started in the mid of the 2010 decade and contextualize it within a longer period (1979–2021), highlighting its extreme character; and (b) through SPI-6, to identify the anomalous dry conditions during wet seasons and to analyze the atmospheric and oceanic patterns associated with it.

Table 1. Summary of the main indices applied to identify droughts in Brazil. A brief description, its limitations, and some work with applications are provided for each index.

Index	Description	Limitation	Application References
Standardized Precipitation Index (SPI)	This index was developed by McKee et al. [45]. It uses historical precipitation data to quantify deficits; positive and negative values are related to wet and dry episodes, respectively; SPI can be calculated and analyzed for accumulated precipitation on scales from 1 to 48 months [10,46].	It does not consider the temperature component, which is important in evapotranspiration processes [6]; therefore, it is more effective for droughts associated with precipitation deficits.	Freitas et al. [15]; Santos et al. [47]; Oliveira-Júnior et al. [48]; Costa et al. [49]; and Silva et al. [50].

Table 1. *Cont.*

Index	Description	Limitation	Application References
Palmer Drought Severity Index (PDSI)	Developed by Palmer [51] to identify droughts affecting crops, it uses precipitation, temperature, and available water content data to measure the loss and demand of the soil moisture supply [10,46].	For its calculation the data series must be complete; and, in addition, there may be lags in identifying dry conditions [46].	Rossato et al. [52]; Silva and Azevedo [53]; Lowe et al. [54]; and Pagotto et al. [55].
Standardized Precipitation–Evapotranspiration Index (SPEI)	Using the SPI base in its calculation, the SPEI, developed by Vicente-Serrano et al. [56], also considers, through the calculation of the water balance, the temperature effect on the development of the drought, making the index sensitive to climate change [10].	Requires temperature and precipitation complete data series; it is calculated from a monthly scale which does not allow the identification of rapidly developed dry conditions [10].	Gozzo et al. [57]; Vega et al. [58]; Drumond et al. [59]; and Rosser et al. [60].
Crop Moisture Index (CMI)	Using precipitation and temperature data, this meteorological index, developed by Palmer [61], is more effective than the PDSI, since it can more efficiently monitor crop conditions in a short period (weeks) [10,46].	It fails to effectively monitor long-term droughts [10,46].	Venteris et al. [62]; Ahammed et al. [63]; and Gonçalves et al. [64].
Deciles and Quintiles	It uses precipitation data, dividing it into equal parts and in ascending order. In Deciles, the precipitation is divided into 10 parts, and in Quintiles into 5. Hence, it is possible to determine the probability of a dry event occurring [10,46].	As with SPI, it does not account for the temperature effects on drought development [10,46].	Silva et al. [65]; Bernardino et al. [66]; Morello et al. [67]; and Aquino et al. [68].
Crop-Specific Drought Indices (CSDI)	Developed by Meyer et al. [69], this index can measure the overall impact on final productivity. For its calculation, data from precipitation, maximum, minimum, and dew point temperature, wind speed, and solar radiation are necessary, as well as information on the available water content and data on the crop [10].	As the input data for the model is complex, not every location has enough records for the calculation to be possible [10].	Martins et al. [70].

2. Materials and Methods

2.1. Study Area

The PHR, also known as Upper Paraná, represents the Brazilian part of the Paraná Basin. Extending from 26°50′ S to 15°25′ S of latitude and 55°55′ W to 43°34′ W of longitude, the PHR covers the Federal District (DF) and six Brazilian states, Santa Catarina (SC), Paraná (PR), São Paulo (SP), Minas Gerais (MG), Mato Grosso do Sul (MS), and Goiás (GO) (Figure 1), and has an approximate area of 879,873 km², about 10% of the entire national territory [16,18].
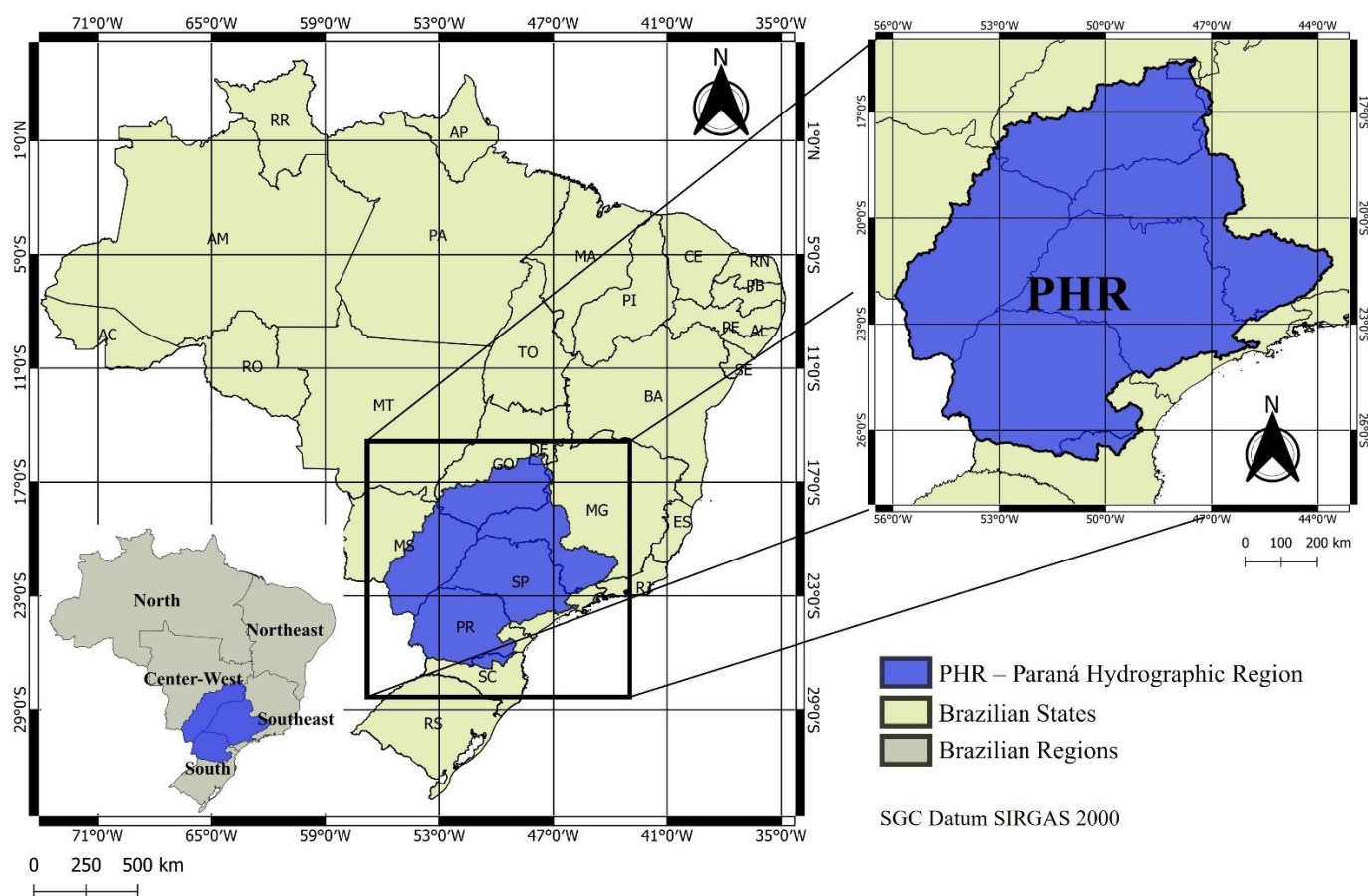
Figure 1. Representation of the study area: on the left side is the location of the PHR inside Brazil, and on the right side, a zoom on the region.

According to IBGE [71], the population in PHR is about 61.3 million inhabitants, concentrating 36% of the country's urban population and 40% of its GDP. In addition, several important Brazilian metropolitan regions are located there, such as: Brasília, Goiânia, Campinas, Curitiba, Maringá, Londrina, and, in particular, the Metropolitan Area of São Paulo, one of the most populous in the world [16–18].

The Paraná River occupies the third place as the longest river in the Americas, but the PHR has only 6% of the national surface water resources available, even though it has the highest water demand in the country [16,17]. The climate patterns of the PHR show significant variations in space and time, which directly affects water availability. Its dominant climate is tropical, except for the south region of the PHR, in the states of Paraná and Santa Catarina, where the temperate subtropical climate predominates [16,17]. The SACZ is known as the main weather system responsible for summer rains [72–74].

2.2. Database

Precipitation data from 1979 to 2021 of the gauge-based analysis of global daily precipitation (CPC) generated by the National Oceanic and Atmospheric Administration/Climate Prediction Center (NOAA/CPC) were used. The CPC interpolates data from surface observations of approximately 30,000 stations distributed across the globe, creating a high-quality unified set that has a spatial resolution of 0.5° [75,76]. Some studies, such as Barreto et al. [77], Jones [78], Torres et al. [79], and Balmaceda-Huarte et al. [80], evaluated and used the CPC database in South America and their results are positive, demonstrating that the precipitation in the region is well represented by the dataset. A time series of monthly rainfall was constructed considering the average rainfall in the blue area indicated in Figure 1. Additionally, from NOAA, the outgoing longwave radiation (OLR) data for the

period 1979 to 2021 were used. They are spatially interpolated data with 1° of horizontal resolution [81].

Datasets from the ERA5 reanalysis [82] provided by the European Center for Medium-Range Weather Forecasts (ECMWF, https://climate.copernicus.eu/climate-reanalysis (accessed on 21 March 2022)) were also used from 1979 to 2021. These datasets have a spatial resolution of 0.25° [82]. The selected variables considered were geopotential height and zonal and meridional wind components at 850 and 250 hPa levels, and sea surface temperature (SST). The 850 hPa level characterizes the circulation of the low-level jet in South America and the SASA; while the 250 hPa level represents the upper-level atmospheric patterns [36,83].

Indices indicative of teleconnection patterns such as the Tropical Southern Atlantic index, Oceanic Niño index, the South Atlantic Subtropical Anticyclone index, Indian Ocean Dipole, Pacific South American indices, and Antarctic Oscillation, were also analyzed and discussed (Table 2).

2.3. Identification of Dry Periods

The method used to identify and characterize dry periods was similar to the one applied by Freitas et al. [15]; however, instead of the SPI on the scale of 1 and 12 months, the SPI was used on the scale of 6 and 12 months to identify anomalous drier conditions prevailing at the semi-annual and annual scales, respectively, in the PHR between 1979 and 2021. As shown in Table 1, SPI uses only precipitation data to identify wet and dry periods on different time scales—more details of the calculation can be found in McKee et al. [45], Silva et al. [50], and Guttman [84]. On the 6-month scale (SPI-6), it can be used to show the variability of precipitation at a semi-annual scale and, on this scale, depending on the region and time of the year, it can be associated with river flows and the levels of reservoir anomalies [6]. The 12-month scale (SPI-12) can be associated with long-term rainfall patterns and anomalies in river flows and reservoir levels [6]. The monthly precipitation data used for the SPI calculations (SPI-6 and SPI-12) did not contain any missing data.

Table 2. Summary of the teleconnection indices used in the study.

Index	Definition	Phase	Impacts on South America Precipitation	Download Source
Tropical Southern Atlantic Index (TSA)	Anomalies of sea surface temperature in the western part of the tropical South Atlantic Ocean [85].	The positive (negative) phase indicates a positive (negative) temperature anomaly over the tropical South Atlantic Ocean region.	The positive (negative) phase of the TSA is associated, in general, with less (more) rain in regions of the south and southeast of Brazil [86].	https://psl.noaa.gov/data/correlation/tsa.data (accessed on 25 September 2022)
Oceanic Niño Index (ONI)	Main monitor, based on SST anomalies in the Niño 3.4 region, of the phases of the El Niño-Southern Oscillation phenomenon [87].	The positive (negative) phase indicates the occurrence of El Niño (La Niña) with warmer (cold) temperatures in the east-central tropical Pacific.	The positive (negative) phase of the ONI is associated with increasing (decreasing) precipitation in the southeastern South America [86].	https://psl.noaa.gov/data/correlation/oni.data (accessed on 25 September 2022)
The South Atlantic Subtropical Anticyclone Index (IASAS)	It allows the analysis of observed surface pressure variations over the south and southeastern Brazil associated with the South Atlantic Subtropical Anticyclone (SASA) [88].	Positive (negative) values indicate higher (lower) pressure at mean sea level in southeast Brazil and lower (higher) in southern Brazil.	The positive (negative) phase of the IASAS is associated with less (more) rain in southeast Brazil and more (less) in the South [88].	https://meteorologia.unifei.edu.br/teleconexoes/indice?id=iasas (accessed on 25 September 2022)

Table 2. *Cont.*

Index	Definition	Phase	Impacts on South America Precipitation	Download Source
Indian Ocean Dipole (IOD)	It characterizes the difference between the sea surface temperature in the western tropical Indian Ocean (Arabian Sea) and the southeastern tropical Indian Ocean, south of Indonesia [89].	In its positive (negative) phase, the western part is warmer (cold) than the southeast.	Its positive (negative) phase is associated with wetter (dry) conditions in southeastern South America [86]	https://meteorologia.unifei.edu.br/teleconexoes/indice?id=iod (accessed on 25 September 2022)
Antarctic Oscillation (AAO)	It indicates the zonal oscillation in the mean sea level pressure (geopotential height etc.) between mid-latitude and the surrounding Antarctica [90,91].	Its positive (negative) phase is associated with negative (positive) anomalies of geopotential height along Antarctica and positive (negative) anomalies in the zonal band around 45°S.	The positive (negative) phase of the AAO contributes to dry (wet) conditions over southern Brazil and wet (dry) conditions in the southeast [86].	https://meteorologia.unifei.edu.br/teleconexoes/indice?id=aao (accessed on 25 September 2022)
Pacific South American (PSA1, PSA2)	While AAO is the first lead mode of EOF applied to different atmospheric variables, PSA1 and PSA2 are the second and third modes. PSA1 and PSA2 allow analyzing the relationship with the wave train that propagates from southeastern Australia to Argentina [91,92].	In Souza and Reboita [88] the positive phase of PSA1 is characterized by positive anomalies of geopotential height over the Pacific reaching the extreme south of South America and negative anomalies covering most of southern South America. In the positive phase of PSA2, southern South America is covered by negative anomalies of geopotential height while south Brazil is covered by positive ones.	The positive phase of PSA1 is associated with increased rainfall in southeastern South America during the austral summer. The positive phase of PSA2, on the other hand, presents precipitation deficits in a region extending from the central region of South America toward the Atlantic Ocean [92].	https://meteorologia.unifei.edu.br/teleconexoes/indice?id=psa1 (PSA1; accessed on 25 September 2022) https://meteorologia.unifei.edu.br/teleconexoes/indice?id=psa2 (PSA2; accessed on 25 September 2022)

McKee et al. [45] created thresholds, as shown in Table 3, to classify the climate conditions represented by the monthly SPI values. The beginning of a drought episode is defined when the SPI value changes from positive to negative and it ends when it returns to positive values; however, the SPI must reach a value equal to or less than −1 to be categorized as a drought event [45]. The severity (absolute sum of all SPI values during the event), duration (number of months between the first and last month of the event), intensity (ratio between severity and duration), and peak (highest absolute value of SPI recorded during the event) may then be calculated according to McKee et al. [45] to characterize the drought events.

Table 3. SPI index classification. Adapted from McKee et al. [45].

SPI	Classification
≥ 2.00	Extremely wet
1.50 to 1.99	Very wet
1.00 to 1.49	Moderately wet
−0.99 to 0.99	Near normal
−1.00 to −1.49	Moderately dry
−1.50 to −1.99	Severely dry
≤ -2.00	Extremely dry

After identifying the hydrological drought event that started in the mid of the 2010 decade through SPI-12, the value of the SPI-6 of March, which is calculated considering data from October of the year prior to March of the present year (which defines the wet season in the region) was considered to identify wet seasons with anomalous dry conditions within the hydrological drought studied. Wet seasons with normal conditions were also identified in the period from 1979 to 2021 using the SPI-6 of March.

2.4. Anomalous Atmospheric and Oceanic Patterns

Monthly anomaly maps were plotted using ERA5 data to investigate atmospheric and oceanic patterns associated with dry weather conditions during the hydrological drought of the mid-2010 decade. Figure 2 summarizes the methodology applied in this paper to calculate the anomaly maps through a flowchart. The variables analyzed were precipitation, SST, OLR, divergent wind at 250 hPa, and stream function at 850 and 250 hPa levels.
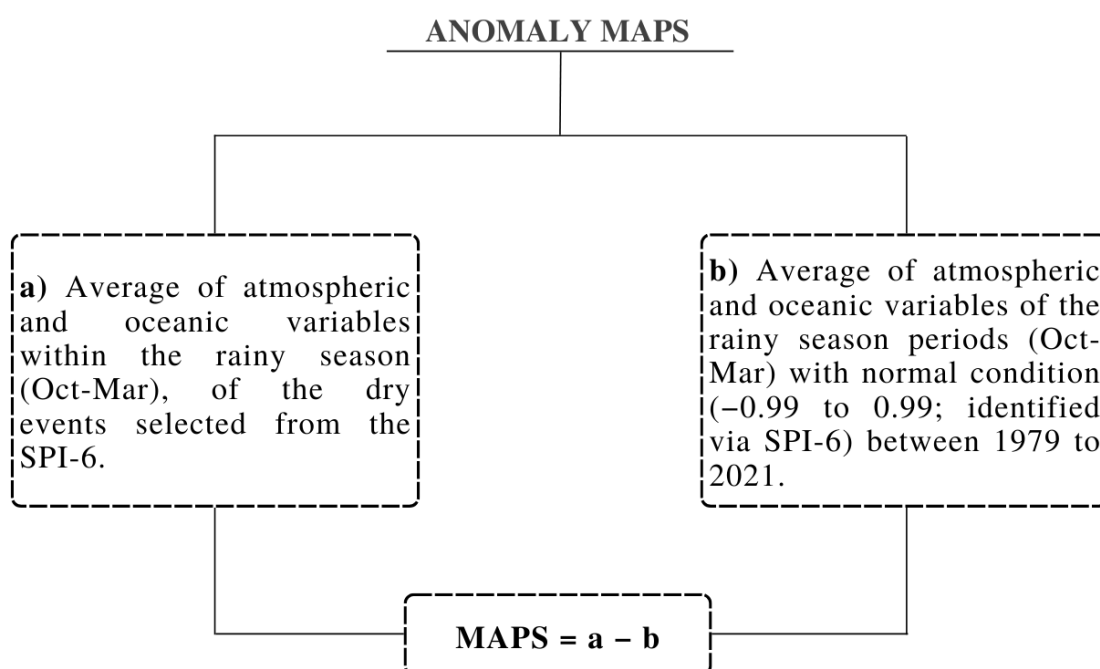

Figure 2. Flowchart summarizing the methodology applied in the present study.

The ray tracing method was applied to verify the propagation path of Rossby waves in the atmospheric composites performed in this study. Details about the methodology can be found in Hoskins and Karoly [93], Hoskins and Ambrizzi [94], and Ferraz [95], while examples of application can be found in Coelho et al. [23] and Müller and Ambrizzi [96]. In a brief view, the method derives from the stationary Rossby's wave propagation theory, which is a ubiquitous feature of atmospheric flow in the upper troposphere [97] and can transfer energy and momentum across great distances and sometimes give rise to patterns of teleconnections [93,98]. For stationary waves, if the total wavenumber increases towards the equator, the curvature in the propagation of the waves will be anticlockwise, but if it increases towards the poles, the curvature becomes clockwise. Ray tracing was used to explore the propagation of Rossby waves with stationary or quasi-stationary phase velocities. These trajectories indicate how information is communicated through the atmosphere over great distances, as well as the time scales on which that information is transmitted. In the cases studied here, we assume that the Rossby wave may be an atmospheric response to a thermal forcing located in a divergence region, according to Hoskins and Karoly [93].

As is well known, there is a general tendency for Rossby waves to be refracted toward the equator due to the sphericity of atmospheric waves [93]. However, the existence of a

zonal jet can change the situation and lead to preferential propagation in the zonal direction. One of the factors favoring the generation of Rossby waves is tropical diabatic heating, which is balanced by upward vertical movement and divergence at high levels, resulting in a disturbance in the absolute vorticity field. Thus, by conservation of absolute vorticity, Rossby waves are generated. Through the analysis of the barotropic vorticity equation, it can be seen that the forcing for Rossby waves is greater in areas where the divergence, the divergent wind, the absolute vorticity, and the absolute vorticity gradient are large. This can happen in regions south (in the southern hemisphere) of warming at the equator, where the upper-level divergence associated with deep convection is greatest and there are large vorticity gradients associated with the subtropical jet. The Western Pacific, east of Australia, is a region that presents such characteristics, thus becoming a favorable region for the formation of Rossby wave trains.

Karoly [99], using the ray tracing technique, showed that in the summer of the southern hemisphere, there is a propagation of Rossby waves with zonal wave numbers from two to four, starting from middle latitudes. As the flow is stronger in the southern hemisphere, the propagation speed is faster than in the northern hemisphere. Hoskins and Ambrizzi [94] and Ambrizzi and Hoskins [100], with a summer state baseline and forcing at 15°S and 105°W, showed that the wave activity propagates across the equator and into North and North Atlantic waveguides. There is also a wave path from the extreme south of South America and the equatorial Atlantic. There is also a path around the tips of South America and Africa and into the equatorial Indian Ocean. These studies show that in addition to the propagation of energy from mid-latitudes, it is possible for Rossby waves to propagate from tropical latitudes, as will be shown in the present study. The standing wave number K_S indicates the regions where Rossby wave propagation is allowed and those where it will be inhibited ($K_S = 0$), highlighting the importance of jets as waveguides. Zonally oriented regions with relatively high K_S values delimited by lower values to the north and south indicate favorable areas for the presence of waveguides, as described in [94]. For this analysis, the average of the Oct–Mar zonal wind of each period identified via SPI-6 was used as a basic state of the atmosphere. The trajectories were simulated considering 6 days of integration and a wave number equal to 3, and those whose endpoint was located in the PHR were chosen.

The average of the values of the climatic indices in the period of Oct–Mar was used to verify which possible teleconnection patterns could be associated with the precipitation patterns.

3. Results and Discussion

3.1. Meteorological Droughts during Hydrological Drought Periods

The monthly and annual precipitation climatology was calculated with data from 1979 to 2021 (Figure 3). The wet season in the PHR was concentrated between the months of October and March, while the months with the lowest rainfall were June, July, and August. The highest rainfall values were concentrated in the southern region of the basin, located in Southern Brazil, where the Itaipu power plant is also located. This region is heavily influenced by transient systems, such as cold fronts, cyclones, and mesoscale convective systems, among others [36,38]. The lowest precipitation values were concentrated in the central and northern part of the basin, mainly between the states of São Paulo and Mato Grosso do Sul, where the monthly precipitation pattern in the region, mainly in the northernmost areas, follows the South American Monsoon System regime, with wetter summer months and drier winter months [36,38].

Applying the SPI-12, four episodes of hydrological droughts in the PHR were identified between 1979 and 2021 (Table 4). The latest event started in November 2016, but its end was not identified, even when the SPI-12 analyses were extended until July 2022. Hence, drought conditions persisted for a time beyond the analyzed period. Table 4 and Figure 4 show that all dry episodes lasted more than 1 year and, over time, the dry events became more severe, with greater duration and intensity. This trend of dry conditions in the SPI-12

agrees with climate studies that indicated a reduction in precipitation in the northernmost regions of the basin [19,20].
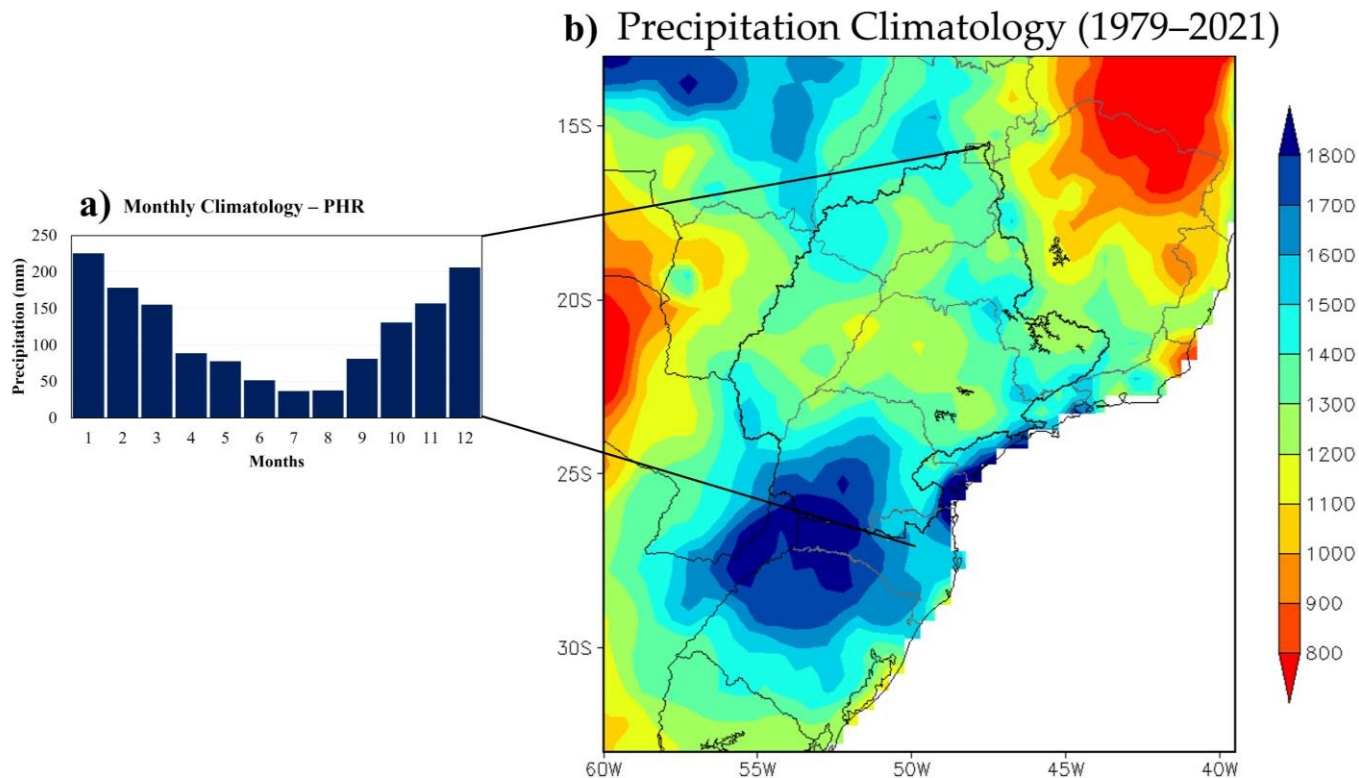

Figure 3. (**a**) Monthly (mm) and (**b**) annual climatology for the PHR, considering the period from 1979 to 2021. The bold black line on the map indicates the PHR data: CPC.

Table 4. Drought hydrological events identified via SPI-12 in the PHR, with their respective parameters defined in Section 2.3. The longest drought episode is highlighted in bold.

Region	Start Date	End Date	Severity	Duration (Months)	Intensity	Peak
	09/1985	11/1986	9.84	15	0.66	1.34
	09/2007	08/2009	15.72	24	0.66	1.46
PHR	12/2011	12/2015	56.94	49	1.16	1.98
	11/2016	**	**88.44**	**62**	**1.43**	**3.88**

** Through December 2021. The end date was not identified as of July 2022.

The two longest and most intense events were: (a) between December 2011 and December 2015 (Table 4), reaching a peak in the absolute value of SPI-12 of 1.98, which gives it the classification of severe drought (Table 3), and (b) the longest and highest peak among all hydrological droughts identified since 1979 is the one started in 2016, which will be the event analyzed in this study. The first drought (a) is documented through several studies [21–24] as being responsible for a serious water crisis with severe impacts in Southeastern Brazil. The second event (b) likely extends beyond the study period, which is limited to December of 2021. Until December of 2021, there were 62 dry months with a SPI-12 peak of 3.88 and classified as an extreme drought (Table 3). Although the values are still partial, this event was the most severe (88.44) and intense (1.43) among all four identified.
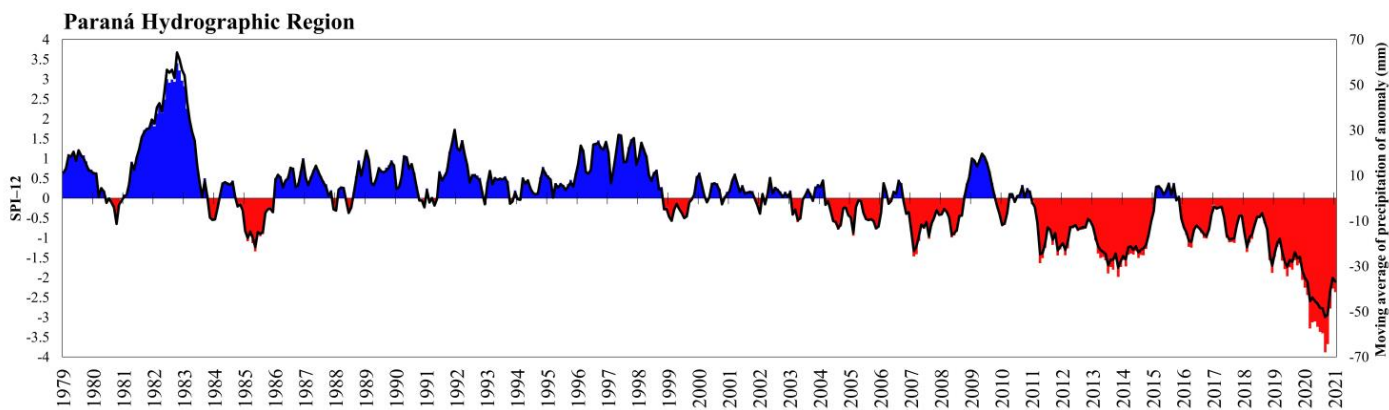
Figure 4. SPI-12 time series, and in the black line, the 12-month moving average of anomalies of precipitation (mm) to PHR.

Through the March SPI-6 values (Figure 5; which refer to the anomalous precipitation conditions accumulated from October of the year prior to March of the present year, which defines the wet season in the region) for the longest and most intense event identified via SPI-12, one can notice the occurrence of three wet seasons anomalously dry (Table 5). The 2016/2017 and 2019/2020 wet seasons presented moderate dry conditions, and, in 2020/2021, they became extreme. Therefore, analyses of the atmospheric and oceanic patterns during the wet seasons (Oct–Mar) of 2016/2017, 2019/2020, and 2020/2021 were carried out.
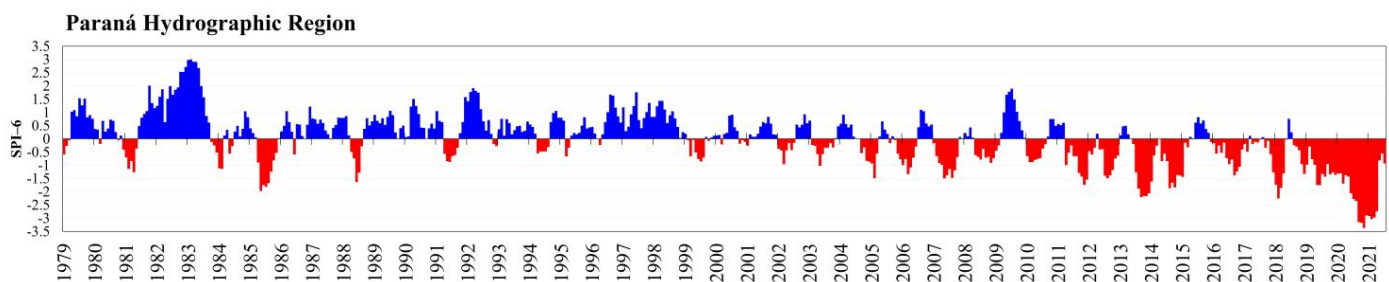

Figure 5. SPI-6 time series for PHR.

Table 5. March SPI-6 values within the hydrological drought event (identified by SPI-12) from 2016 to 2021. The years marked in bold were characterized by moderate or extreme drought conditions (identified by SPI-6).

YEAR	SPI-6 MAR (OCT–MAR)
2015/2016	0.37
2016/2017	−**1.23**
2017/2018	−0.08
2018/2019	−0.43
2019/2020	−**1.35**
2020/2021	−**3.17**

3.2. Anomalous Atmospheric and Oceanic Patterns

Between the years 2016 and 2021, three wet seasons anomalously dry were identified, as indicated by the SPI-6. A spatial representation of the precipitation anomalies in each one of them and the wind anomalies at 850 hPa to infer the transport of moisture by low-level jets (LLJ) in the atmosphere is shown in Figure 6. In all of these composites, it is noted that the scarcity of rain is related to southeastern wind anomalies over PHR. These anomalous winds seem to be associated with the weakening of the LLJ east of the Andes, over the

PHR, as well as the weakening of the northeast wind over Center-West and southeastern Brazil. As discussed in previous studies [101–103], the LLJ is a modulator of the SACZ and, consequently, of the rainy season. Therefore, the question that arises is: which mechanisms may be acting to weaken the LLJ and hinder the transport of moisture from the tropical region to the subtropics?
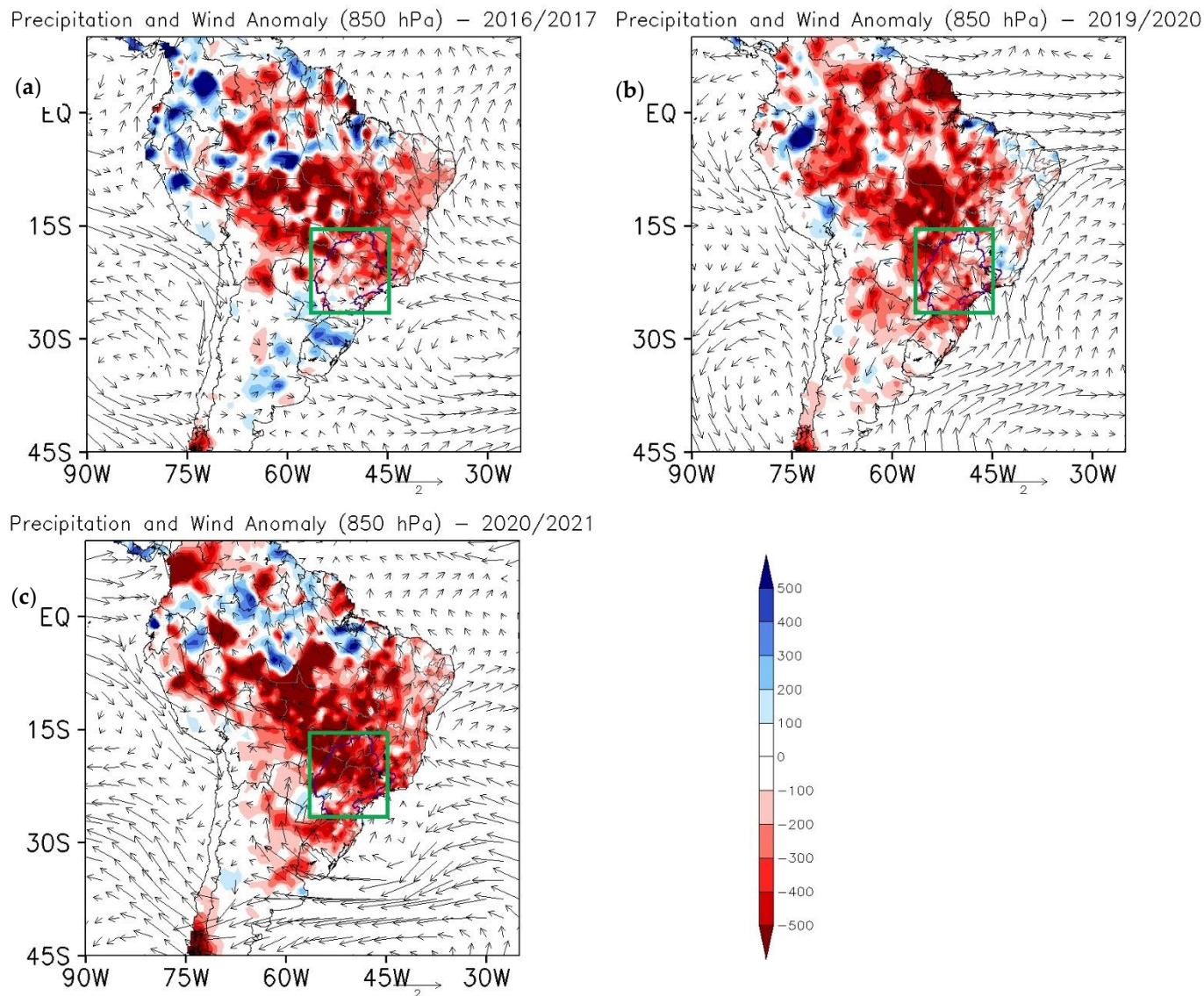

Figure 6. Anomalies of precipitation (mm) and wind at 850 hPa (reference vector is 2 m s^{-1}), considering the subtraction of the rainy season (Oct–Mar average) of 2016/2017 (**a**), 2019/2020 (**b**), and 2020/2021 (**c**) from the normal conditions registered during Oct–Mar (1979-2021); (**a**) monthly (mm) and (**b**) annual climatology for the PHR, considering the period from 1979 to 2021. The bold green box on the map indicates the PHR. Data source: CPC.

To answer the question, (i) the divergent wind anomalies at 250 hPa, OLR anomalies, and wave trajectories (Figure 7a), and (ii) stream function anomalies at 250 and 850 hPa (Figure 7b,c) are presented. These fields help to identify large-scale wave patterns that may be associated with different teleconnection mechanisms. Negative (positive) values of the stream function anomaly indicate regions with an anticyclonic (cyclonic) anomaly in the southern hemisphere. The atmospheric and oceanic patterns during the three analyzed periods are not similar (Figure 7a,b) and the beginning of wave propagation also slightly

differs. Despite that, in all cases, the waves have genesis in a region of divergent wind at 250 hPa (figure not shown), which is also indicated by the anomalies field (Figure 7a).
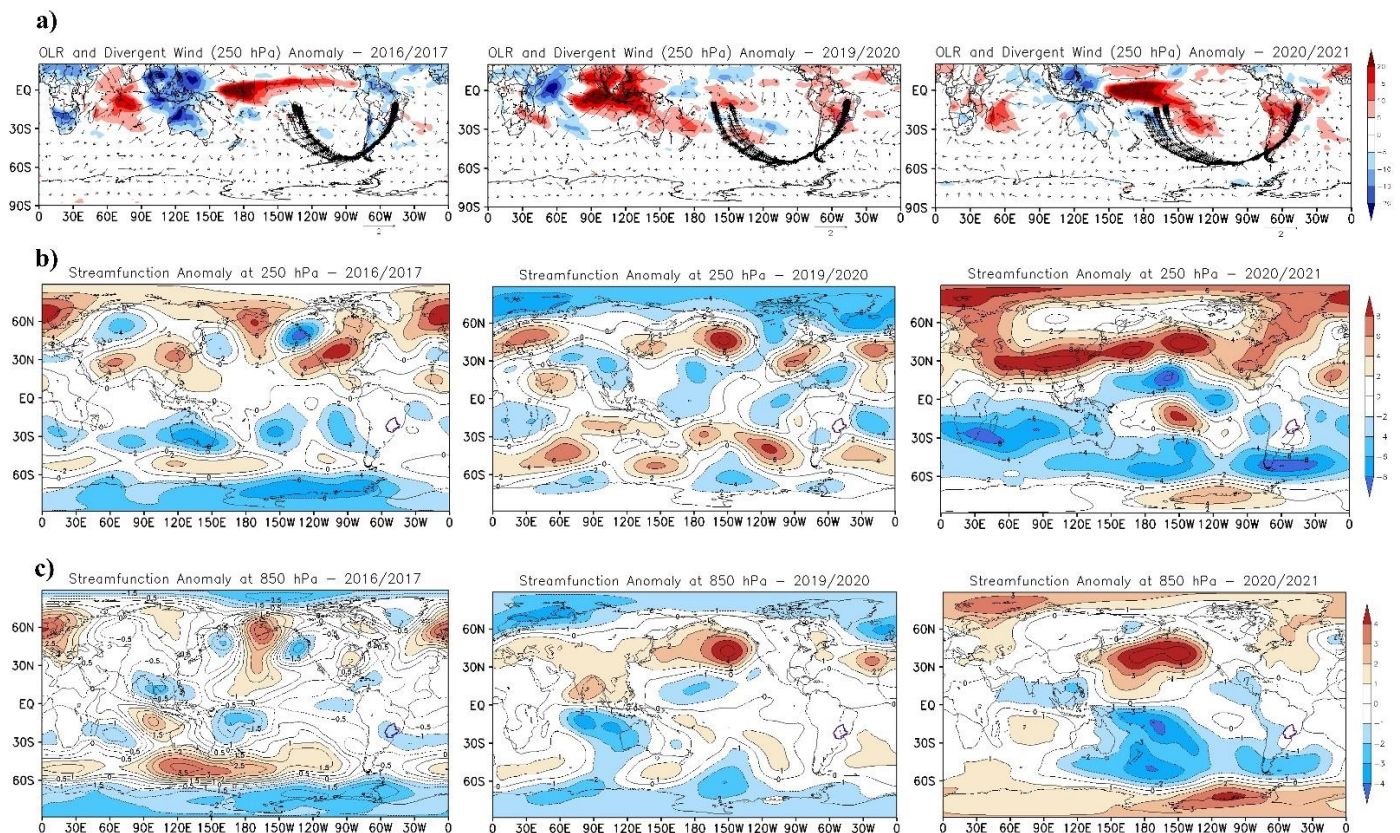

Figure 7. (**a**) OLR and divergent wind anomaly (250 hPa); stream function anomaly for levels (**b**) 250 hPa and (**c**) 850 hPa. The fields were plotted considering the subtraction of the Oct–Mar average, within the hydrological drought event, from the Oct–Mar climatology (1979–2021). The PHR is highlighted by a purple line and the wave train is indicated by the black dashed lines.

3.2.1. Drought 2016/2017

In 2016/2017, the ray tracing analysis (Figure 7a) indicates a wave pattern propagating from warmer SST in the central Southern Pacific Ocean (Figure 8) in a region of anomalous divergent wind at 250 hPa, near longitude 130°W, toward South America (Figure 7a). The propagation of this wave apparently contributes to a negative stream function anomaly (anticyclonic circulation anomaly) at 850 hPa between the PHR and the Atlantic Ocean (Figure 7c). The presence of anticyclonic circulation in the mentioned region inhibits the flow of the LLJ from the Amazon region to it. Thus, less moisture ends up being transported to PHR, resulting in less rainfall in the region. It seems to be a possible explanation for the configuration of the dry conditions in 2016/2017.

The association of this result with the teleconnection patterns (Table 6) seems to be a combination of factors. Positive IASAS (0.28) indicates that SASA is well configured over southeastern Brazil, inhibiting precipitation (high pressure anomaly inhibits the LLJ displacement from tropical to subtropical region) in this area, and favors rainfall in southern Brazil, which can be seen in Figure 6a. Positive TSA (0.39) can contribute with subsidence over southeastern Brazil, which disfavors cloud organization. Weak negative ONI (-0.40), in general, is considered as a neutral phase of El Niño, but the Niño index in region 1+2 (west coast of Peru and Chile; not shown in Table 6) in the same period was strongly positive, which may contribute with the positive precipitation anomaly over extreme southern Brazil (Figure 6a), and this signal can be coupled with the negative AAO index (-0.53). Regarding PSA1 and PSA2, these indices were very weak.
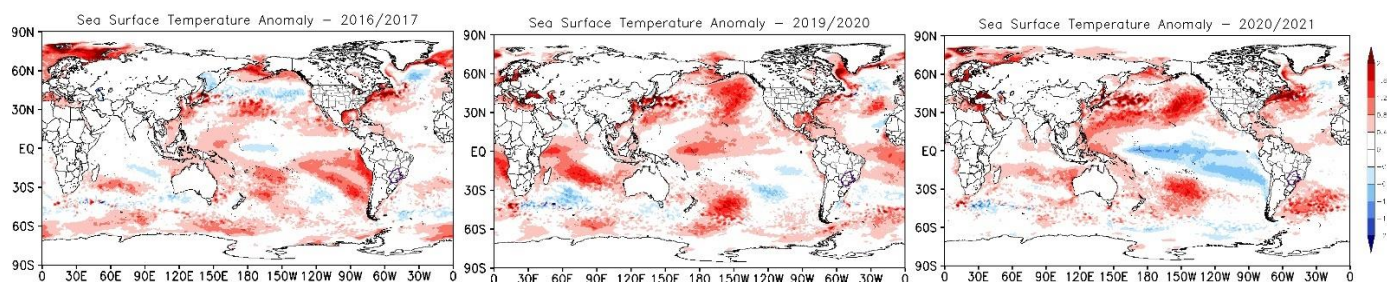
Figure 8. SST anomaly considering the subtraction of the Oct–Mar average, within the hydrological drought event, from the Oct–Mar climatology (1979–2021). This field was plotted for 2016/2017, 2019/2020, and 2020/2021 events.

Table 6. Values of the March SPI-6, and the average of the monthly values of the IASAS, TSA, ONI, IOD, AAO, PSA1, and PSA2 indices for the Oct–Mar periods classified as moderate, severe, or extreme dry conditions (identified by the SPI-6), during the hydrological drought event (identified by SPI-12) for the PHR. The standard deviation (SD) of the indices was obtained from the website: https://meteorologia.unifei.edu.br/teleconexoes/ (accessed on 21 March 2022). The indices that surpass the SD are highlighted in bold.

Periods	SPI-6	IASAS (SD ± 1.164)	TSA (SD ± 0.38)	ONI (SD ± 0.5)	IOD (SD ± 0.34)	AAO (SD ± 0.98)	PSA1 (SD ± 0.18)	PSA2 (SD ± 0.12)
2016/2017	−1.23	0.28	**0.39**	−0.40	−0.02	−0.53	−0.02	−0.11
2019/2020	−1.35	−0.23	**0.89**	0.47	**0.48**	−0.44	−0.05	−0.01
2020/2021	−3.17	−0.62	0.11	−**1.08**	0.21	**1.01**	−0.01	−0.03

3.2.2. Drought 2019/2020

During 2019/2020 (Figure 7a–c), the origin of the wave trajectory that reached PHR was in the central Pacific Ocean (approximately in the longitude of 150°W and latitude of 10°S), slightly displaced westwards when compared to 2016/2017 (Figure 7a). This wave pattern reached the Subtropical Atlantic with a positive stream function anomaly at 850 hPa (Figure 7c) and 250 hPa (Figure 7b) and with a pattern resembling a convergence in the divergent wind anomalies at 250 hPa; suggesting a barotropic structure of the atmosphere (same pattern of anomalies dominate in the atmosphere column). The presence of a cyclonic anomaly in the Subtropical Atlantic Ocean, near the south/southeast coast, can be an indicator of the SASA weakening and a driver of the stagnation/weakening of the moisture transport towards from Amazon to the PHR. Indeed, Table 6 shows a negative value for IASAS (−0.23), which is an indicator of the SASA weakening near southeastern Brazil. It is also interesting to note that the SASA weakening predominates a south wind anomaly along the south Brazilian coast with a rotation to northwest over southeastern Brazil. This anomalous flow should contribute as a source of moisture to the continent, but it is not shown through the precipitation anomalies (Figure 6b). A suggestion here is that other mechanisms are acting to inhibit precipitation, as will be discussed. At 250 hPa (Figure 7b), there are two anomalous anticyclonic centers located to the southwest and northeast of PHR. This pattern may favor air subsidence movements over PHR, consequently, preventing the formation of rain clouds, which can be verified in the positive values of OLR (Figure 7a). In addition, the positive TSA index (0.89) can produce additional subsidence, and the coupling strengthens the subsidence.

During the analyzed season, the ONI index indicated neutral conditions (0.47), but this value is close to the threshold of 0.5 (El Niño condition), and from OND to JFM it is 0.5. These values support the pattern of positive SST anomalies (Figure 8) in the Equatorial Pacific resembling the occurrence of a weak El Niño, which could induce atmospheric teleconnection patterns to South America and impact the PHR. However, this pattern is still very much distinct from that in the other two analyzed drought periods. In neutral

periods regarding El Niño and La Niña and with AAO negative phase, southern Brazil is wetter and southeastern Brazil is dryer than in the normal or in La Niña periods [86]. Indeed, Figure 6b shows more intense negative anomalies of precipitation over central and southeastern Brazil than in the south region. Regarding PSA1 and PSA2, these indices were very weak.

The IOD (0.48) and TSA (0.89) were in their positive phases, while the other indices were neutral (Table 6). The positive TSA is related to a weaker SASA. Weaker southeasterly trade winds from the SASA (Figure 6) cause less friction on the ocean reducing the evaporation [104], which implies a SST warming (Figure 8) over the tropical South Atlantic. Although we do not analyze the evaporation, these physical processes are in agreement with the stream function anomalies (Figure 7c), which show cyclonic anomalies between tropical and subtropical Atlantic Ocean, or in other words, a weaker SASA. In relation to IOD, following different studies [86,105] and their online Atlas (https://meteorologia.unifei.edu.br/teleconexoes/atlas/?ind=IOD&var=precwnd850; accessed on 25 September 2022), the positive IOD phase can contribute to the dry conditions in the north sector of the PHR during the austral spring and summer seasons. In Chan et al. [105], the Rossby wave train that leads to dry conditions over the PHR and central Brazil extends from the subtropical south Indian Ocean to the subtropical South Atlantic and causes an anomalous intensification of the SASA and, consequently, the anomalous anticyclone in the lower troposphere causes anomalous divergence of moisture over central Brazil. Our results in part are in agreement with this author, since the wave train over the Pacific Ocean resembles their wave train, but in the Atlantic Ocean, we observed anomalous cyclonic circulation and a weakening of the SASA (which were in agreement with the TSA pattern). The difference in the source of the wave train in both studies can be associated with the method applied; we used ray tracing, while Chan et al. [105] used a linear barotropic model based on the vorticity equation. Our method has some limitations, such as the fact that the ray tracing method only identifies the wave's path outside the tropics. As in the present study, there are negative anomalies of OLR (Figure 7a) and positive anomalies of SST (Figure 8) in the western Indian Ocean. We can suggest that the source of the wave train is the Indian Ocean, but our methodology was only able to identify it over the Pacific Ocean. This hypothesis deserves to be investigated in a future study.

3.2.3. Drought 2020/2021

For 2020/2021, there was a wave path starting in the western Pacific (Figure 7a), in a region of strong divergent wind anomaly at 250 hPa, near 170°W longitude. This wave reached South America with negative stream function anomalies at 850 hPa (Figure 7c) and 250 hPa (Figure 7b), which characterizes a barotropic atmospheric pattern. The negative stream function anomaly near the northwest sector of PHR is indicative of air subsidence, causing difficulties in cloud formation. While in the stream function anomaly (Figure 7c), it is not so clear a cyclonic circulation near the coast of south–southeastern Brazil, this feature is better represented by the wind anomaly in Figure 6c, indicating a weakening of the SASA, which is also an agent in the transport of moisture from the ocean to the continent during the rainy season, because it is far from the continent (displaced to the ocean) [38,106]. South of this cyclonic anomaly, there is another covering all the southern of South America. This dipole pattern can be linked with the positive phase of AAO. This phase is characterized by negative anomalies of mean sea level pressure around Antarctica, positive ones in the mid-latitudes, and by negative anomalies over the South Atlantic Ocean, closer to the Brazilian coast. It can lead to the SASA deconfiguration contributing to the negative IASAS (−0.62) in Table 6.

La Niña also predominated during the 2020/2021 wet season (−1.08, Table 6), which inhibits rainfall in Southern Brazil [86,107] by weakening the LLJ and negatively impacting the volume of rainfall in Southern Brazil [86,108,109]. The negative anomalies of stream function over the oceans around southern South America allow the SST to become warmer (southern 30°S; Figure 8). In addition, as positive anomalies of mean sea level pressure

near Argentina are dominant during positive AAO (1.01), it would act to hinder the passage of frontal systems and also weaken the post-frontal cold air mass, leading to less precipitation in the SUB. In summary, in this analyzed period, the deficit of precipitation can be mainly associated with La Niña and positive AAO phase. Finally, PSA1 and PSA2 showed weak values.

4. Conclusions

This study showed, via SPI-12, the hydrological droughts in PHR, and the most extreme episode in the period 1979–2021 was analyzed. The longest and most severe drought in the PHR started in November 2016, and until December 2021, did not end after 62 months of drought.

The SPI-6 revealed three rainy seasons during this drought event marked by anomalous dry conditions during the hydrological drought, for which the analysis of atmospheric and oceanic patterns was deepened (2016/2017, 2019/2020, and 2020/2021). In general, the patterns identified differ from each other: (a) in 2016/2017, a large-scale wave pattern propagated from the central Pacific Ocean towards South America (Figure 9a) and was associated with a positive anticyclonic anomaly off the coast of Brazil that weakened the LLJ and consequently inhibited the transport of moisture from the Amazon towards the basin; this period was characterized by positive SST anomalies near the Peru and Chile coasts (El Niño considering the Niño 1+2 index); (b) in 2019/2020, the pattern of waves coming from the western Pacific towards South America potentially favored subsidence movements of the air over the basin region in addition to the weakening of the SASA that potentially weakened the transport of moisture from the LLJ, impacting the volume of rainfall in the PHR; in this drought period El Niño–Southern Oscillation was in the neutral period; and (c) in 2020/2021, as in the other cases, there was a de-intensification of the LLJ caused by the occurrence of La Niña and the positive phase of the AAO, which de-intensified the SASA, impacting the transport of moisture from the Amazon region to the PHR. During this season, the wave propagation pattern was similar to the one found in 2019/2020, starting in the western Pacific (Figure 9c). However, the presence of a negative stream function anomaly over South America, the action of La Niña, and the positive phase of the AAO, potentially hindered the passage of cold fronts and helped to weaken the LLJ, which disfavors the flow coming from the Amazon region, ceasing the mechanisms that could cause rain in the region. Thus, despite the large-scale patterns not being similar, they have in common the weakening of the LLJ, making it more difficult for moisture transport to the PHR.

Droughts were studied in a regionalized way in the country; however, the results found in this study indicate recent drought events affecting several regions of Brazil simultaneously. Finally, the results suggest that it is not possible to identify a single pattern responsible for the drought. This indicates that, for a better interpretation of atmospheric patterns, and consequently, a better climate forecast, the performance of specialized professionals is essential.

The PHR, being one of the main Brazilian basins, ends up suffering from socioeconomic impacts when drought events occur. Therefore, it is important to identify physical mechanisms that contribute to these anomalies in atmospheric circulation patterns. It is not always possible to determine the forcing of waves in the atmosphere, but in this study, we tried to understand how anomalies are associated with large-scale patterns. The ray tracing method only identifies the wave path in the extratropical region, so it is suggested that the wave is propagating from the tropical region, and when it reaches the extratropical sector, it is traced, which can be better investigated with different tools in a future study. We emphasize that the objective of the work was to analyze the atmospheric and oceanic patterns associated with the anomalous dry rainy seasons recorded during the extreme drought event between the years 2016 and 2021. Thus, the patterns found in the events of 2016/2017, 2019/2020, and 2020/2021 cannot be considered the unique significant sample to determine a precise mechanism of how anomalous atmospheric and oceanic patterns

contribute to the extreme drought conditions in the basin. Therefore, a more climatic perspective of droughts is important and can also be addressed in future work.
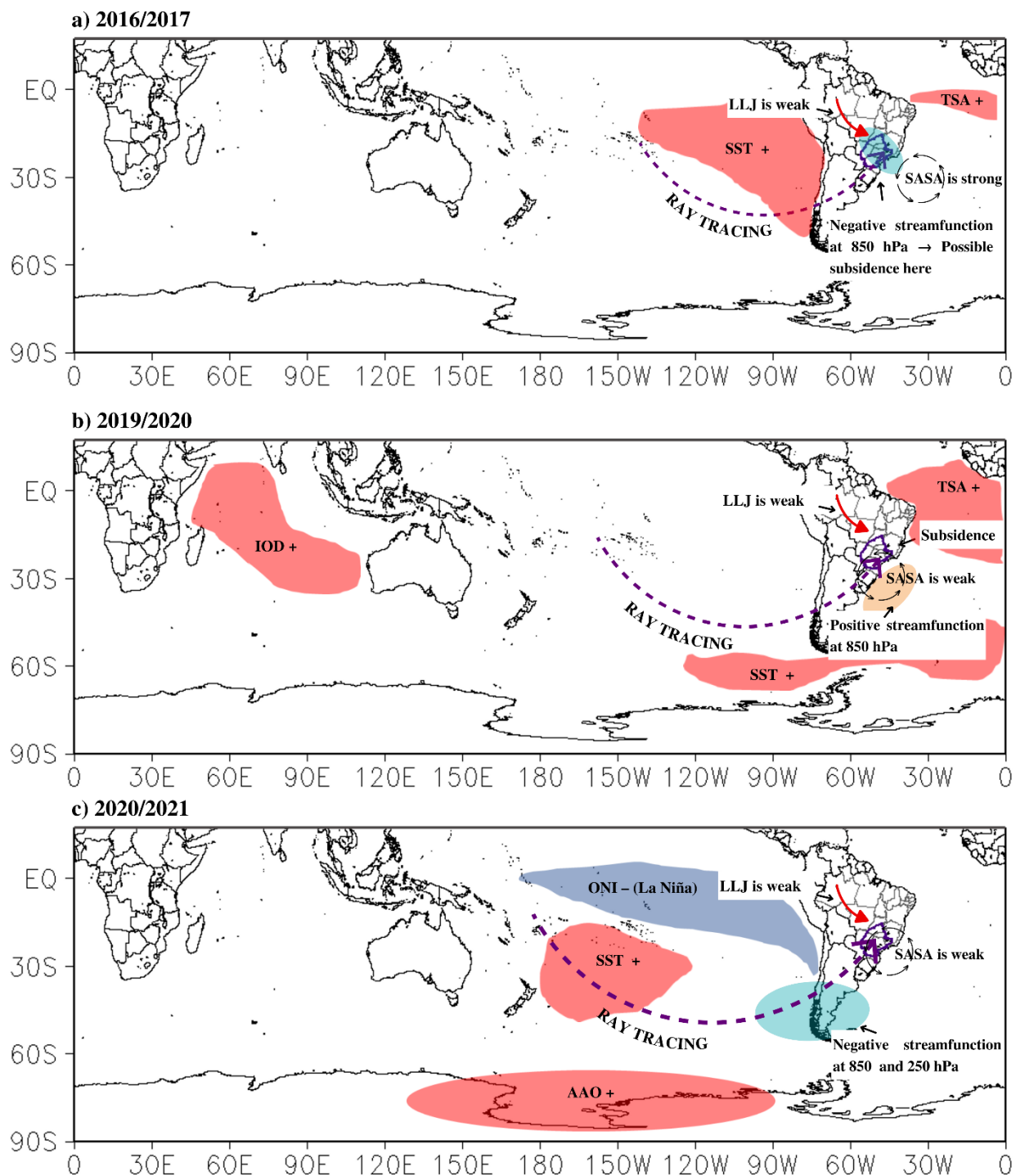

Figure 9. Scheme of atmospheric and oceanic patterns associated with droughts in the PHR for the periods: (**a**) 2016/2017; (**b**) 2019/2020; and (**c**) 2020/2021.

References

1. NASEM—National Academies of Sciences, Engineering, and Medicine. *Attribution of Extreme Weather Events in the Context of Climate Change*; The National Academies Press: Washington, DC, USA, 2016. [CrossRef]
2. IPCC—Intergovernmental Panel on Climate Change. Climate Change 2021: The Physical Science Basis. Summary for Policymakers. Contribution of Working Group I to the Sixth Assessment Report of the Intergovernmental Panel on Climate Change. 2021. Available online: https://www.ipcc.ch/report/ar6/wg1/ (accessed on 2 February 2022).
3. Reboita, M.S.; Kuki, C.A.C.; Marrafon, V.H.; De Souza, C.A.; Ferreira, G.W.S.; Teodoro, T.; Lima, J.W.M. South America climate change revealed through climate indices projected by GCMs and Eta-RCM ensembles. *Clim. Dyn.* **2021**, *58*, 459–485. [CrossRef]
4. WMO—World Meteorological Organization. *Atlas of Mortality and Economic Losses From Weather, Climate and Water Extremes (1970–2019)*; World Meteorological Organization: Geneva, Switzerland, 2021. Available online: https://library.wmo.int/index.php?lvl=notice_display&id=21930#.Yy8l2HaZPrc (accessed on 19 July 2022).
5. CEPED. Atlas Brasileiro de Desastres Naturais 1991 a 2012. Florianópolis: CEPED UFSC. 2013. Available online: https://www.ceped.ufsc.br/wp-content/uploads/2012/01/AMAZONAS_mioloWEB.pdf (accessed on 26 January 2022).
6. WMO—World Meteorological Organization. Standardized Precipitation Index. User Guide. 2012. Available online: https://library.wmo.int/doc_num.php?explnum_id=7768 (accessed on 10 February 2022).
7. Van Loon, A.F.; Gleeson, T.; Clark, J.; Van Dijk, A.I.J.M.; Stahl, K.; Hannaford, J.; Baldasarre, G.; Teuling, A.J.; Tallaksen, L.M.; Uijlenhoet, R.; et al. Drought in the Anthropocene. *Nat. Geosci.* **2016**, *9*, 89–91. [CrossRef]
8. Wilhite, D.A.; Glantz, M.H. Understanding: The drought phenomenon: The role of definitions. *Water Int.* **1985**, *10*, 111–120. [CrossRef]
9. Schadeck, R. (Org). Relatório de Danos Materiais e Prejuízos Decorrentes de Desastres Naturais no Brasil: 1995–2019/Banco Mundial. Global Facility for Disaster Reduction and Recovery. Fundação de Amparo à Pesquisa e Extensão Universitária. Centro de Estudos e Pesquisas em Engenharia e Defesa Civil. 2 ed. Florianópolis: FAPEU. 2020. Available online: https://www.gov.br/mdr/pt-br/centrais-de-conteudo/publicacoes/protecao-e-defesa-civil-sedec/danos_e_prejuizos_versao_em_revisao.pdf (accessed on 15 February 2022).
10. WMO—World Meteorological Organization; GWP—Global Water Partnership. *Handbook of Drought Indicators and Indices*; World Meteorological Organization: Geneva, Switzerland, 2016. Available online: https://public.wmo.int/en/resources/library/handbook-of-drought-indicators-and-indices (accessed on 25 January 2022).
11. Silva, S.M.; Souza Filho, F.A.; Araújo, L.M., Jr. Mecanismo financeiro projetado com índices de seca como instrumento de gestão de risco em recursos hídricos. *Rev. Bras. De Recur. Hidr.* **2015**, *20*, 320–330. Available online: https://abrh.s3.sa-east-1.amazonaws.com/Sumarios/157/b916a3b776ef816b1c8b6d4f20737176_be9ff1352a9be9d30ef8a1cf001e09f1.pdf (accessed on 7 December 2021). [CrossRef]
12. Brito, S.S.B.; Cunha, A.P.M.; Cunningham, C.C.; Alvalá, R.C.; Marengo, J.A.; Carvalho, M.A. Frequency, duration and severity of drought in the Semiarid Northeast Brazil region. *Int. J. Climatol.* **2017**, *38*, 517–529. [CrossRef]
13. Cunha, A.P.M.A.; Zeri, M.; Leal, K.D.; Costa, L.; Cuartas, L.A.; Marengo, J.A.; Tomasella, J.; Vieira, R.M.; Barbosa, A.A.; Cunningham, C.; et al. Extreme drought events over Brazil from 2011 to 2019. *Atmosphere* **2019**, *10*, 642. [CrossRef]
14. Xavier, L.C.P.; Silva, S.M.O.D.; Carvalho, T.M.N.; Pontes Filho, J.D.; Souza Filho, F.D.A.D. Use of Machine Learning in Evaluation of Drought Perception in Irrigated Agriculture: The Case of an Irrigated Perimeter in Brazil. *Water* **2020**, *12*, 1546. [CrossRef]
15. Freitas, A.A.; Drumond, A.; Carvalho, V.S.B.; Reboita, M.S.; Silva, B.C.; Uvo, C.B. Drought Assessment in São Francisco River Basin, Brazil: Characterization through SPI and Associated Anomalous Climate Patterns. *Atmosphere* **2022**, *13*, 41. [CrossRef]
16. MMA—Ministério do Meio Ambiente. *Caderno da Região Hidrográfica do Paraná/Ministério do Meio Ambiente, Secretaria de Recursos Hídricos*; MMA: Brasília, 2006. Available online: https://www.yumpu.com/pt/document/view/39998037/parana-caderno-da-regiao-hidrografica-ministerio-do- (accessed on 12 April 2022).
17. ANA—Agência Nacional De Águas E Saneamento Básico. *Atlas Brasil: Abastecimento Urbano de água: Panorama Nacional*; ANA: Brasília, 2010. Available online: https://www.aris.sc.gov.br/uploads/revista/2735/YXwFOHqcDQSDQEA2bJfi2KfS2Pt-Binw.pdf (accessed on 25 January 2022).

18. ANA—Agência Nacional De Águas E Saneamento Básico. *Conjuntura dos Recursos Hídricos no Brasil: Regiões Hidrográficas Brasileiras—Edição Especial*; ANA: Brasíli, 2015. Available online: https://www.snirh.gov.br/portal/centrais-de-conteudos/conjuntura-dos-recursos-hidricos/regioeshidrograficas2014.pdf (accessed on 3 March 2022).

19. Rafee, S.A.A.; Freitas, E.D.; Martins, J.A.; Martins, L.D.; Domingues, L.M.; Nascimento, J.M.P.; Machado, C.B.; Santos, E.B.; Rudke, A.P.; Fujita, T.; et al. Spatial trends of extreme precipitation events in the paraná river basin. *J. Appl. Meteorol. Climatol.* **2020**, *59*, 443–454. [CrossRef]

20. Cuartas, L.A.; Cunha, A.P.M.A.; Alves, J.A.; Parra, L.M.P.; Deusdará-Leal, K.; Costa, L.C.O.; Molina, R.D.; Amor, D.; Broedel, E.; Seluchi, M.H.; et al. Recent Hydrological Droughts in Brazil and Their Impact on Hydropower Generation. *Water* **2022**, *14*, 601. [CrossRef]

21. Marengo, J.A.; Nobre, C.A.; Seluchi, M.E.; Cuartas, A.; Alves, L.M.; Mendiondo, E.M.; Obregón, G.; Sampaio, G. A seca e a crise hídrica de 2014-2015 em São Paulo. *Rev. USP* **2015**, *106*, 31–44. [CrossRef]

22. Coelho, C.A.S.; De Oliveira, C.P.; Ambrizzi, T.; Reboita, M.S.; Carpenedo, C.B.; Campos, J.L.P.S.; Tomaziello, A.C.N.; Pampuch, L.A.; Custódio, M.S.; Dutra, L.M.M.; et al. The 2014 southeast Brazil austral summer drought: Regional scale mechanisms and teleconnections. *Clim. Dyn.* **2015**, *46*, 3737–3752. [CrossRef]

23. Coelho, C.A.S.; Cardoso, D.H.F.; Firpo, M.A. A seca de 2013 a 2015 na região sudeste do Brasil. *Climanálise* **2016**, 55–66. Available online: http://climanalise.cptec.inpe.br/~{}rclimanl/revista/pdf/30anos/Coelhoetal.pdf (accessed on 12 May 2022).

24. Finke, K.; Jiménez-Esteve, B.; Taschetto, A.S.; Ummenhofer, C.C.; Bumke, K.; Domeisen, D.I.V. Revisiting remote drivers of the 2014 drought in South-Eastern Brazil. *Clim. Dyn.* **2020**, *55*, 3197–3211. [CrossRef] [PubMed]

25. Itaipu Binacional. Assegurar o Acesso Confiável, Sustentável, Moderno e a Preço Acessível à Energia Para Todas e Todos/Itaipu Binacional. Dirección de Coordinación Ejecutiva; Diretoria de Coordenação; Central Hidrelétrica de Itaipu: Itaipu Binacional. 2019. Available online: https://www.itaipu.gov.br/sites/default/files/af_df/Estudo_de_caso_Itaipu_ODS_7.pdf (accessed on 11 March 2022).

26. Itaipu Binacional. Relatório Anual Itaipu Binacional 2020. Foz do Iguaçu, Paraná. 2020. Available online: https://www.itaipu.gov.br/sites/default/files/af_df/RELATORIO_ITAIPU_2020.pdf (accessed on 11 March 2022).

27. Fernandes, V.R.; Cunha, A.P.M.A.; Pineda, L.A.C.; Leal, K.R.D.; Costa, L.C.O.; Broedel, E.; França, D.A.; Alvalá, R.C.S.; Seluchi, M.E.; Marengo, J. Secas e os impactos na região sul do brasil. *Rev. Bras. De Climatol.* **2021**, *28*, 561–584. [CrossRef]

28. Gomes, M.S.; Cavalcanti, I.F.A.; Müller, G.V. 2019/2020 drought impacts on South America and atmospheric and oceanic influences. *Weather Clim. Extrem.* **2021**, *34*, 100404. [CrossRef]

29. Naumann, G.; Podesta, G.; Marengo, J.; Luterbacher, J.; Bavera, D.; Muñoz, C.A.; Barbosa, P.; Cammalleri, C.; Chamorro, L.; Cuartas, A.; et al. *The 2019–2021 Extreme Drought Episode in La Plata Basin*; EUR 30833 EN; Publications Office of the European Union: Luxembourg, 2021.

30. ANA—Agência Nacional De Águas E Saneamento Básico. ANA Declara Situação Crítica de Escassez Quantitativa dos Recursos Hídricos da Região Hidrográfica do Paraná. 2022. Available online: https://agenciabrasil.ebc.com.br/geral/noticia/2021-06/ana-declara-situacao-critica-na-regiao-hidrografica-do-parana (accessed on 20 March 2022).

31. DH—Departamento Hidroviário. Hidrovia Tietê-Paraná. 2022. Available online: http://www.dh.sp.gov.br/hidrovia-tiete-parana/ (accessed on 21 March 2022).

32. DM—Diário da Manhã. Retomada de Navegação Tietê-Paraná Favorece Goiás. 2022. Available online: https://www.dm.com.br/economia/2022/03/retomada-de-navegacao-tiete-parana-favorece-goias/ (accessed on 21 March 2022).

33. ECONÔMICO VALOR. Navegação na Hidrovia Tietê-Paraná Será Retomada Hoje. 2022. Available online: https://valor.globo.com/agronegocios/noticia/2022/03/15/navegacao-na-hidrovia-tiete-parana-sera-retomada-hoje.ghtml (accessed on 21 March 2022).

34. FOLHA DE S.PAULO. Navegação na Hidrovia Tietê-Paraná Será Retomada Após seca. 2022. Available online: https://www1.folha.uol.com.br/colunas/painelsa/2022/03/navegacao-na-hidrovia-tiete-parana-sera-retomada-apos-seca.shtml?aff_source=56d95533a8284936a374e3a6da3d7996 (accessed on 21 March 2022).

35. G1. Hidrovia Tietê-Paraná tem Data Marcada Para Retomada da Navegação Após Estiagem Suspender Operações. 2022. Available online: https://g1.globo.com/sp/bauru-marilia/noticia/2022/03/11/hidrovia-tiete-parana-tem-data-marcada-para-retomada-da-navegacao-apos-estiagem-suspender-operacoes.ghtml (accessed on 21 March 2022).

36. Reboita, M.S.; Gan, M.A.; Da Rocha, R.P.D.; Ambrizzi, T. Regimes de precipitação na América do Sul: Uma revisão bibliográfica. *Rev. Bras. De Meteorol.* **2010**, *25*, 185–204. [CrossRef]

37. Reboita, M.S.; Krusche, N.; Ambrizzi, T.; Rocha, R.P.D. Entendendo o Tempo e o Clima na América do Sul. 2012. Available online: https://www.ppegeo.igc.usp.br/index.php/TED/article/view/8401/7672 (accessed on 9 December 2022).

38. Ferreira, G.W.S.; Reboita, M.S. A New Look into the South America Precipitation Regimes: Observation and Forecast. *Atmosphere* **2022**, *13*, 873. [CrossRef]

39. Salton, F.G.; Morais, H.; Lohmann, M. Períodos Secos no Estado do Paraná. *Rev. Bras. De Meteorol.* **2021**, *36*, 295–303. [CrossRef]

40. Marengo, J.A. O futuro clima do Brasil. *Rev. USP* **2014**, *103*, 25–32. [CrossRef]

41. PBMC—Painel Brasileiro de Mudanças Climáticas. *Base Científica das Mudanças Climáticas. Contribuição do Grupo de Trabalho 1 do Painel Brasileiro de Mudanças Climáticas ao Primeiro Relatório da Avaliação Nacional sobre Mudanças Climáticas*; Ambrizzi, T., Araujo, M., Eds.; COPPE. Universidade Federal do Rio de Janeiro: Rio de Janeiro, RJ, Brasil, 2014; p. 464. Available online: http://www.pbmc.coppe.ufrj.br/documentos/RAN1_completo_vol1.pdf (accessed on 14 April 2022).

42. Lyra, A.; Tavares, P.; Chou, S.C.; Sueiro, G.; Dereczynski, C.; Sondermann, M.; Silva, A.; Marengo, J.; Giarolla, A. Climate change projections over three metropolitan regions in Southeast Brazil using the non-hydrostatic Eta regional climate model at 5-km resolution. *Theor. Appl. Climatol.* **2017**, *132*, 663–682. [CrossRef]

43. Reboita, M.S.; Marrafon, V.H.A.; Llopart, M.; Da Rocha, R.P. Cenários de mudanças climáticas projetados para o estado de Minas Gerais. *Rev. Bras. Climatol.* **2018**, *1*, 110–128. [CrossRef]

44. ANA—Agência Nacional De Águas E Saneamento Básico. *Mudanças Climáticas e Recursos Hídricos: Avaliações e Diretrizes Para Adaptação/Agência Nacional de Águas*; ANA/GGES: Brasília, 2016. Available online: https://cdn.agenciapeixevivo.org.br/media/2019/06/MudancasClimaticaseRecursosHidricos.pdf (accessed on 4 May 2022).

45. Mckee, T.B.; Doesken, N.J.; Kleist, J. The relationship of drought frequency and duration to time scales. In Proceedings of the 8th Conference on Applied Climatology; 1993; pp. 179–183. Available online: https://climate.colostate.edu/pdfs/relationshipofdroughtfrequency.pdf (accessed on 10 November 2021).

46. Fernandes, D.S.; Heinemann, A.B.; Da Paz, R.L.; Amorim, A.O.; Cardoso, A.S. Índices para a quantificação da seca. Embrapa Arroz e Feijão-Documentos (INFOTECA-E). 2009. Available online: https://www.infoteca.cnptia.embrapa.br/bitstream/doc/663874/1/doc244.pdf (accessed on 10 November 2021).

47. Santos, S.R.Q.; Braga, C.C.; Sansigolo, C.A.; Santos, A.P.P. Determinação de regiões homogêneas do índice de precipitação normalizada (SPI) na Amazônia Oriental. *Rev. Bras. De Meteorol.* **2017**, *32*, 111–122. [CrossRef]

48. Oliveira-Júnior, J.F.; Gois, G.; Terassi, P.M.B.; Silva Junior, C.A.; Blanco, C.J.C.; Sobral, B.S.; Gasparini, K.A.C. Drought severity based on the SPI index and its relation to the ENSO and PDO climatic variability modes in the regions North and Northwest of the State of Rio de Janeiro-Brazil. *Atmos. Res.* **2018**, *212*, 91–105. [CrossRef]

49. Costa, M.D.S.; Oliveira-Júnior, J.F.D.; Santos, P.J.D.; Correia Filho, W.L.F.; Gois, G.D.; Blanco, C.J.C.; Teodoro, P.E.; Silva Junior, C.A.; Santiago, D.B.; Souza, E.O.; et al. Rainfall extremes and drought in Northeast Brazil and its relationship with El Niño–Southern Oscillation. *Int. J. Climatol.* **2020**, *41*, E2111–E2135. [CrossRef]

50. Da Silva, D.F.; Lima, M.J.S.; Souza Neto, P.F.; Gomes, H.B.; Silva, F.D.S.; Almeida, H.R.R.C.; Pereira, M.P.S.; Costa, R.L. Caracterização de eventos extremos e de suas causas climáticas com base no índice Padronizado de Precipitação Para o Leste do Nordeste. *RBGF* **2020**, *13*, 449–464. [CrossRef]

51. Palmer, W.C. *Meteorological Drought*; US Department of Commerce, Weather Bureau: Washington, DC, USA, 1965.

52. Rossato, L.; Marengo, J.A.; Angelis, C.F.D.; Pires, L.B.M.; Mendiondo, E.M. Impact of soil moisture over Palmer Drought Severity Index and its future projections in Brazil. *RBRH* **2017**, *22*, E36. [CrossRef]

53. Silva, F.J.B.C.; Azevedo, J.R.G. Temporal trend of drought and aridity indices in semi-arid pernambucano to determine susceptibility to desertification. *RBRH* **2020**, *25*, e32. [CrossRef]

54. Lowe, R.; Lee, S.A.; O'reilly, K.M.; Brady, O.J.; Bastos, L.; Carrasco-Escobar, G.; Catão, R.C.; Colón-González, F.J.; Barcellos, C.; Carvalho, M.S.; et al. Combined effects of hydrometeorological hazards and urbanisation on dengue risk in Brazil: A spatiotemporal modelling study. *Lancet Planet. Health* **2021**, *5*, e209–e219. [CrossRef]

55. Pagotto, M.A.; Menezes, I.R.N.; Costa, C.M.; Lisi, C.S.; Bräuning, A. Oxygen isotopes in tree rings of Cedrela odorata L. as an indicator of hydroclimate variations in a seasonally dry tropical forest in northeastern Brazil. *Trees* **2021**, *35*, 1889–1903. [CrossRef]

56. Vicente-Serrano, S.M.; Beguería, S.; López-Moreno, J.I. A multiscalar drought index sensitive to global warming: The standardized precipitation evapotranspiration index. *J. Clim.* **2010**, *23*, 1696–1718. [CrossRef]

57. Gozzo, L.F.; Palma, D.S.; Custodio, M.S.; Machado, J.P. Climatology and trend of severe drought events in the state of São Paulo, Brazil, during the 20th century. *Atmosphere* **2019**, *10*, 190. [CrossRef]

58. Vega, H.M.; Lima, J.R.; Cerniak, S.N. SPEI and Hurst analysis of precipitation in the Amazonian Area of Brazil. *Rev. Bras. De Meteorol.* **2019**, *34*, 325–334. [CrossRef]

59. Drumond, A.; Stojanovic, M.; Nieto, R.; Gimeno, L.; Liberato, M.L.R.; Pauliquevis, T.; Oliveira, M.; Ambrizzi, T. Dry and Wet Climate Periods over Eastern South America: Identification and Characterization through the SPEI Index. *Atmosphere* **2021**, *12*, 155. [CrossRef]

60. Rosser, J.I.; Nielsen-Saines, K.; Saad, E.; Fuller, T. Reemergence of yellow fever virus in southeastern Brazil, 2017–2018: What sparked the spread? *PLoS Negl. Trop. Dis.* **2022**, *16*, e0010133. [CrossRef]

61. Palmer, W.C. Keeping track of crop moisture conditions, nationwide: The new crop moisture index. *Weatherwise* **1968**, *21*, 156–161. [CrossRef]

62. Venteris, E.R.; Tagestad, J.D.; Downs, J.L.; Murray, C.J. Detection of anomalous crop condition and soil variability mapping using a 26 year Landsat record and the Palmer crop moisture index. *Int. J. Appl. Earth Obs. Geoinf.* **2015**, *39*, 160–170. [CrossRef]

63. Ahammed, S.J.; Homsi, R.; Khan, N.; Shahid, S.; Shiru, M.S.; Mohsenipour, M.; Ahmed, K.; Nawaz, N.; Alias, N.E.; Yuzir, A. Assessment of changing pattern of crop water stress in Bangladesh. *Environ. Dev. Sustain.* **2019**, *22*, 4619–4637. [CrossRef]

64. Gonçalves, S.T.N.; Vasconcelos Junior, F.D.C.; Sakamoto, M.S.; Silveira, C.D.S.; Martins, E.S.P.R. Índices e Metodologias de Monitoramento de Secas: Uma Revisão. *Rev. Bras. Meteorol.* **2021**, *36*, 495–511. [CrossRef]

65. Silva, B.B.D.; Ferreira, M.A.; Silva, V.D.P.; Ferreira, R.D.C. Desempenho de modelo climático aplicado à precipitação pluvial do Estado de Pernambuco. *Rev. Bras. De Eng. Agrícola E Ambient.* **2010**, *14*, 387–395. [CrossRef]

66. Bernardino, B.S.; Vasconcellos, F.C.; Nunes, A.M.B. Impact of the equatorial Pacific and South Atlantic SST anomalies on extremes in austral summer precipitation over Grande river basin in Southeast Brazil. *Int. J. Climatol.* **2018**, *38*, e131–e143. [CrossRef]

67. Morello, T.F.; Ramos, R.M.; Anderson, L.O.; Owen, N.; Rosan, T.M.; Steil, L. Predicting fires for policy making: Improving accuracy of fire brigade allocation in the Brazilian Amazon. *Ecol. Econ.* **2020**, *169*, 106501. [CrossRef]

68. Aquino, D.N.; Andrade, E.M.D.A.M.; Tavares, E.T.D.S.F.; Campos, D.A.C.A. Impacto de Secas e Antropização na Dinâmica da Cobertura Florestal em Fragmento do Domínio Fitogeográfico da Caatinga. *Rev. Bras. De Geogr. Física* **2021**, *14*, 1675–1689. [CrossRef]

69. Meyer, S.J.; Hubbard, K.G.; Wilhite, D.A. A crop-specific drought index for corn: I. Model development and validation. *Agron. J.* **1993**, *85*, 388–395. [CrossRef]

70. Martins, M.A.; Tomasella, J.; Rodriguez, D.A.; Alvalá, R.C.S.; Giarolla, A.; Garofolo, L.L.; Siqueira, J.L., Jr.; Paolicchi, L.T.L.C.; Pinto, G.L.N. Improving drought management in the Brazilian semiarid through crop forecasting. *Agric. Syst.* **2018**, *160*, 21–30. [CrossRef]

71. IBGE—Instituto Brasileiro de Geografia e Estatística. Censo de 2010. 2010. Available online: http://www.ibge.gov.br/home/estatistica/populacao/censo2010/default.shtm (accessed on 9 December 2021).

72. Silva, D.F.; Brito, J.I.B. Variabilidade do vento na bacia hidrográfica do rio São Francisco durante a ocorrência da ZCAS. *AMBIÊNCIA* **2008**, *4*, 221–235. Available online: https://revistas.unicentro.br/index.php/ambiencia/article/view/164 (accessed on 13 December 2021).

73. Reboita, M.S.; Marietto, D.M.G.; Souza, A.; Barbosa, M. Caracterização atmosférica quando da ocorrência de eventos extremos de chuva na região sul de Minas Gerais. *Rev. Bras. De Climatol.* **2017**, *21*, 20–37. [CrossRef]

74. Escobar, G.C.J.; Reboita, M.S. Relationship between daily atmospheric circulation patterns and South Atlantic Convergence Zone (SACZ) events. *Atmósfera*. 2020. Available online: https://www.revistascca.unam.mx/atm/index.php/atm/article/view/52936 (accessed on 10 November 2021).

75. Chen, M.; Shi, W.; Xie, P.; Silva, V.B.S.; Kousky, V.E.; Higgins, R.W.; Janowiak, J.E. Assessing objective techniques for gauge-based analyses of global daily precipitation. *J. Geophys. Res. Atmos.* **2008**, *113*, 1–13. [CrossRef]

76. Sun, Q.; Miao, C.; Duan, Q.; Ashouri, H.; Sorooshian, S.; Hsu, K. A review of global precipitation data sets: Data sources, estimation, and intercomparisons. *Rev. Geophys.* **2018**, *56*, 79–107. [CrossRef]

77. Barreto, N.J.; Cavalcanti, I.F.; Mesquita, M.D.; Pedra, G.U. Multivariate intraseasonal rainfall index applied to South America. *Meteorol. Appl.* **2019**, *26*, 521–527. [CrossRef]

78. Jones, C. Recent changes in the South America low-level jet. *Npj Clim. Atmos. Sci.* **2019**, *2*, 20. [CrossRef]

79. Torres, F.L.R.; Ferreira, G.W.S.; Kuki, C.A.C.; Vasconcellos, B.T.C.; Freitas, A.A.; Silva, P.N.; Souza, C.A.; Reboita, M.S. Validação de Diferentes Bases de Dados de Precipitação nas Bacias Hidrográficas do Sapucaí e São Francisco. *Rev. Bras. Climatol.* **2020**, *27*, 368–404.

80. Balmaceda-Huarte, R.; Olmo, M.E.; Bettolli, M.L.; Poggi, M.M. Evaluation of multiple reanalyses in reproducing the spatio-temporal variability of temperature and precipitation indices over southern South America. *Int. J. Climatol.* **2021**, *41*, 5572–5595. [CrossRef]

81. Liebmann, B.; Smith, C.A. Description of a complete (interpolated) outgoing longwave radiation dataset. *Bull. Am. Meteorol. Soc.* **1996**, *77*, 1275–1277.

82. Hersbach, H.; Dee, D. "ERA-5 Reanalysis Is in Production". ECMWF Newsletter, Number 147, Spring 2016. p. 7. Available online: https://www.ecmwf.int/sites/default/files/elibrary/2016/16299-newsletter-no147-spring-2016.pdf (accessed on 13 May 2022).

83. Vasquez, T. *Weather Analysis & Forecasting Handbook*, 5th ed.; Weather Graphics Technologies: Garland, TX, USA, 2002.

84. Guttman, N.B. Comparing the palmer drought index and the standardized precipitation index 1. *J. Am. Water Resour. Assoc.* **1998**, *34*, 113–121. [CrossRef]

85. Enfield, D.B.; Mestas-Nuñez, A.M.; Mayer, D.A.; Cid-Serrano, L. How ubiquitous is the dipole relationship in tropical Atlantic sea surface temperatures? *J. Geophys. Res. Ocean.* **1999**, *104*, 7841–7848. [CrossRef]

86. Reboita, M.S.; Ambrizzi, T.; Crespo, N.M.; Dutra, L.M.M.; Ferreira, G.W.D.S.; Rehbein, A.; Drumond, A.; De Rocha, R.P.; De Souza, C.A.D. Impacts of teleconnection patterns on South America climate. *Ann. N. Y. Acad. Sci.* **2021**, *1504*, 116–153. [CrossRef]

87. NOAA—National Oceanic and Atmospheric Administration. Climate Variability: Oceanic Niño Index. 2009. Available online: https://www.climate.gov/news-features/understanding-climate/climate-variability-oceanic-ni%C3%B1o-index (accessed on 12 August 2022).

88. De Souza, C.A.; Reboita, M.S. Ferramenta para o monitoramento dos padrões de teleconexão na América do Sul. *TerraE Didat.* **2021**, *17*, e02109. [CrossRef]

89. Saji, N.H.; Yamagata, T.J.C.R. Possible impacts of Indian Ocean dipole mode events on global climate. *Clim. Res.* **2003**, *25*, 151–169. [CrossRef]

90. Mo, K.C. Relationships between low-frequency variability in the Southern Hemisphere and sea surface temperature anomalies. *J. Clim.* **2000**, *13*, 3599–3610. [CrossRef]

91. Thompson, D.W.J.; Wallace, J.M. Annular modes in the extratropical circulation. Part I: Month-to-month variability. *J. Clim.* **2000**, *13*, 1000–1016. [CrossRef]

92. Mo, K.C.; Paegle, J.N. The Pacific–South American modes and their downstream effects. *Int. J. Climatol. A J. R. Meteorol. Soc.* **2001**, *21*, 1211–1229. [CrossRef]

93. Hoskins, B.J.; Karoly, D.J. The steady linear response of a spherical atmosphere to thermal and orographic Forcing. *J. Atmos. Sci.* **1981**, *38*, 1179–1196. [CrossRef]

94. Hoskins, B.J.; Ambrizzi, T. Rossby wave propagation on a realistic longitudinally varying flow. *J. Atmos. Sci.* **1993**, *50*, 1661–1671. [CrossRef]

95. Ferraz, S.E.T. Variabilidade Intrasazonal no Brasil e Sul da América do Sul. Ph.D. Thesis, Universidade de São Paulo, São Paulo, São Paulo, Brazil, 2004.

96. Müller, G.V.; Ambrizzi, T. Rossby wave propagation tracks in southern hemisphere mean basic flows associated to generalized frosts over southern South America. *Atmósfera* **2010**, *23*, 25–35. Available online: https://www.scielo.org.mx/scielo.php?pid=S0187-62362010000100002&script=sci_abstract&tlng=pt (accessed on 19 September 2022).

97. Rossby, C.G. Planetary flow pattern in the atmosphere. *Q. J. R. Meteorol. Soc.* **1940**, *66*, 68–87. Available online: https://empslocal.ex.ac.uk/people/staff/gv219/classics.d/Rossby-planflowQJ40.pdf (accessed on 9 December 2022).

98. Branstator, G. Circumglobal teleconnections, the jet stream waveguide, and the North Atlantic Oscillation. *J. Clim.* **2002**, *15*, 1893–1910. Available online: https://journals.ametsoc.org/view/journals/clim/15/14/1520-0442_2002_015_1893_cttjsw_2.0.co_2.xml (accessed on 9 December 2022). [CrossRef]

99. Karoly, D.J. Rossby wave propagation in a barotropic atmosphere. *Dyn. Atmos. Ocean.* **1983**, *7*, 111–125. [CrossRef]

100. Ambrizzi, T.; Hoskins, B.J. Stationary Rossby-wave propagation in a baroclinic atmosphere. *Q. J. R. Meteorol. Soc.* **1997**, *123*, 919–928. [CrossRef]

101. Nogués-Paegle, J.; Mo, K.C. Alternating wet and dry conditions over South America during summer. *Mon. Weather Rev.* **1997**, *125*, 279–291. [CrossRef]

102. Carvalho, L.M.V.; Jones, C.; Liebmann, B. The South Atlantic convergence zone: Intensity, form, persistence, and relationships with intraseasonal to interannual activity and extreme rainfall. *J. Clim.* **2004**, *17*, 88–108. [CrossRef]

103. Silva, J.P.R.; Reboita, M.S.; Escobar, G.C.J. Caracterização da Zona de Convergência do Atlântico Sul em campos atmosféricos recentes. *Rev. Bras. De Climatol.* **2019**, *25*, 355–377. [CrossRef]

104. Tanimoto, Y.; Xie, S.P. Inter-hemispheric decadal variations in SST, surface wind, heat flux and cloud cover over the Atlantic Ocean. *J. Meteorol. Soc. Jpn.* **2002**, *80*, 1199–1219. [CrossRef]

105. Chan, S.C.; Behera, S.K.; Yamagata, T. Indian Ocean dipole influence on South American rainfall. *Geophys. Res. Lett.* **2008**, *35*, L14S12. [CrossRef]

106. Reboita, M.S.; Ambrizzi, T.; Silva, B.A.; Pinheiro, R.F.; Rocha, R.P. The South Atlantic subtropical anticyclone: Present and future climate. *Front. Earth Sci.* **2019**, *7*, 8. [CrossRef]

107. Cai, W.; Mcphaden, M.J.; Grimm, A.M.; Rodrigues, R.R.; Taschetto, A.S.; Garreaud, R.D.; Dewitte, B.; Poveda, G.; Ham, Y.; Santoso, A.; et al. Climate impacts of the El Niño–southern oscillation on South America. *Nat. Rev. Earth Environ.* **2020**, *1*, 215–231. [CrossRef]

108. Grimm, A.M.; Barros, V.R.; Doyle, M.E. Climate variability in southern South America associated with El Niño and La Niña events. *J. Clim.* **2000**, *13*, 35–58. Available online: https://www.ige.unicamp.br/terraedidatica/v8-1/pdf81/s3.pdf (accessed on 9 December 2022). [CrossRef]

109. Silva, G.A.M.; Ambrizzi, T.; Marengo, J.A. Observational evidences on the modulation of the South American Low Level Jet east of the Andes according the ENSO variability. In *Annales Geophysicae*; Copernicus GmbH, 2009; pp. 645–657. Available online: https://angeo.copernicus.org/articles/27/645/2009/ (accessed on 9 December 2022).